Multiview Neural Surface Reconstruction by Disentangling Geometry and Appearance

Lior Yariv   **Yoni Kasten**   **Dror Moran**

Meirav Galun   **Matan Atzmon**   **Ronen Basri**   **Yaron Lipman**

Weizmann Institute of Science

{lior.yariv, yoni.kasten, dror.moran, meirav.galun, matan.atzmon, ronen.basri, yaron.lipman}@weizmann.ac.il

Abstract

In this work we address the challenging problem of multiview 3D surface reconstruction. We introduce a neural network architecture that simultaneously learns the unknown geometry, camera parameters, and a neural renderer that approximates the light reflected from the surface towards the camera. The geometry is represented as a zero level-set of a neural network, while the neural renderer, derived from the rendering equation, is capable of (implicitly) modeling a wide set of lighting conditions and materials. We trained our network on real world 2D images of objects with different material properties, lighting conditions, and noisy camera initializations from the DTU MVS dataset. We found our model to produce state of the art 3D surface reconstructions with high fidelity, resolution and detail.

1 Introduction

Learning 3D shapes from 2D images is a fundamental computer vision problem. A recent successful neural network approach to solving this problem involves the use of a (neural) differentiable rendering system along with a choice of (neural) 3D geometry representation. Differential rendering systems are mostly based on ray casting/tracing [50, 40, 28, 30, 46, 31], or rasterization [32, 23, 10, 29, 4], while popular models to represent 3D geometry include point clouds [58], triangle meshes [4], implicit representations defined over volumetric grids [20], and recently also neural implicit representations, namely, zero level sets of neural networks [30, 40].

The main advantage of implicit neural representations is their flexibility in representing surfaces with arbitrary shapes and topologies, as well as being mesh-free (i.e., no fixed a-priori discretization such as a volumetric grid or a triangular mesh). Thus far, differentiable rendering systems with implicit neural representations [30, 31, 40] did not incorporate lighting and reflectance properties required for producing faithful appearance of 3D geometry in images, nor did they deal with trainable camera locations and orientations.

The goal of this paper is to devise an end-to-end neural architecture system that can learn 3D geometries from masked 2D images and rough camera estimates, and requires no additional supervision, see Figure 1. Towards that end we represent the color of a pixel as a differentiable function in the three unknowns of a scene: the geometry, its appearance, and the cameras. Here, appearance means collectively all the factors that define the surface light field, *excluding* the geometry, i.e., the surface bidirectional reflectance distribution function (BRDF) and the scene's lighting conditions. We call this architecture the Implicit Differentiable Renderer (IDR). We show that IDR is able to approximate the light reflected from a 3D shape represented as the zero level set of a neural network. The approach can handle surface appearances from a certain restricted family, namely, all surface light fields that can be represented as continuous functions of the point on the surface, its normal, and the viewing direction. Furthermore, incorporating a global shape feature vector into IDR increases its ability to handle more complex appearances (e.g., indirect lighting effects).

IDR

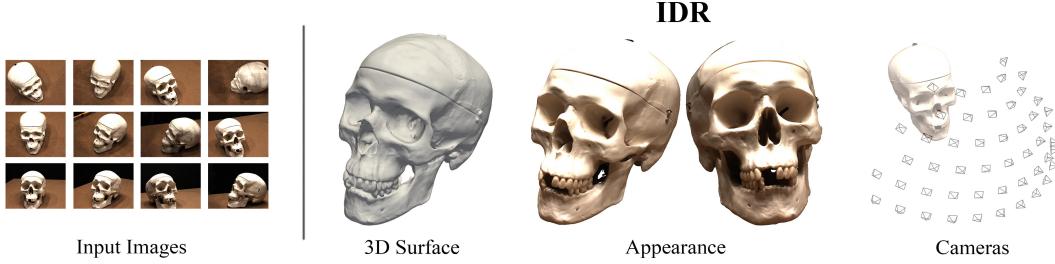| Input Images | 3D Surface | Appearance | Cameras |

Figure 1: We introduce IDR: end-to-end learning of geometry, appearance and cameras from images.

Most related to our paper is [40], that was first to introduce a fully differentiable renderer for implicit neural occupancy functions [37], which is a particular instance of implicit neural representation as defined above. Although their model can represent arbitrary color and texture, it cannot handle general appearance models, nor can it handle unknown, noisy camera locations. For example, we show that the model in [40], as-well-as several other baselines, fail to generate the Phong reflection model [8]. Moreover, we show experimentally that IDR produces more accurate 3D reconstructions of shapes from 2D images along with accurate camera parameters. Notably, while the baseline often produces shape artifact in specular scenes, IDR is robust to such lighting effects. Our code and data are available at `https://github.com/lioryariv/idr`.

To summarize, the key contributions of our approach are:

- End-to-end architecture that handles unknown geometry, appearance, and cameras.
- Expressing the dependence of a neural implicit surface on camera parameters.
- Producing state of the art 3D surface reconstructions of different objects with a wide range of appearances, from real-life 2D images, with both exact and noisy camera information.

2 Previous work

Differentiable rendering systems for learning geometry comes (mostly) in two flavors: differentiable rasterization [32, 23, 10, 29, 4], and differentiable ray casting. Since the current work falls into the second category we first concentrate on that branch of works. Then, we will describe related works for multi-view surface reconstruction and neural view synthesis.

Implicit surface differentiable ray casting. Differentiable ray casting is mostly used with *implicit* shape representations such as implicit function defined over a volumetric grid or implicit neural representation, where the implicit function can be the occupancy function [37, 5], signed distance function (SDF) [42] or any other signed implicit [2]. In a related work, [20] use a volumetric grid to represent an SDF and implement a ray casting differentiable renderer. They approximate the SDF value and the surface normals in each volumetric cell. [31] use sphere tracing of pre-trained DeepSDF model [42] and approximates the depth gradients w.r.t. the latent code of the DeepSDF network by differentiating the individual steps of the sphere tracing algorithm; [30] use field probing to facilitate differentiable ray casting. In contrast to these works, IDR utilize exact and differentiable surface point and normal of the implicit surface, and considers a more general appearance model, as well as handle noisy cameras.

Multi-view surface reconstruction. During the capturing process of an image, the depth information is lost. Assuming known cameras, classic Multi-View Stereo (MVS) methods [9, 48, 3, 54] try to reproduce the depth information by matching features points across views. However, a post-processing steps of depth fusion [6, 36] followed by the Poisson Surface Reconstruction algorithm [24] are required for producing a valid 3D watertight surface reconstruction. Recent methods use a collection of scenes to train a deep neural models for either sub-tasks of the MVS pipeline, e.g., feature matching [27], or depth fusion [7, 44], or for an End-to-End MVS pipeline [16, 56, 57]. When the camera parameters are unavailable, and given a set of images from a specific scene, Structure From Motion (SFM) methods [51, 47, 22, 19] are applied for reproducing the cameras and a sparse 3D reconstruction. Tang and Tan [53] use a deep neural architecture with an integrated differentiable Bundle Adjustment [55] layer to extract a linear basis for the depth of a reference frame, and features from nearby images and to optimize for the depth and the camera parameters in each forward pass. In contrast to these works, IDR is trained with images from a single target scene, producing an accurate watertight 3D surface reconstruction.

Neural representation for view synthesis. Recent works trained neural networks to predict novel views and some geometric representation of 3D scenes or objects, from a limited set of images with known cameras. [50] encode the scene geometry using an LSTM to simulate the ray marching process. [38] use a neural network to predict volume density and view dependent emitted radiance to synthesis new views from a set of images with known cameras. [41] use a neural network to learns the surface light fields from an input image and geometry and predicting unknown views and/or scene lighting. Differently from IDR, these methods do not produce a 3D surface reconstruction of the scene's geometry nor handle unknown cameras.

3 Method

Our goal is to reconstruct the geometry of an object from masked 2D images with possibly rough or noisy camera information. We have three unknowns: (i) *geometry*, represented by parameters $\theta \in \mathbb{R}^m$; (ii) *appearance*, represented by $\gamma \in \mathbb{R}^n$; and (iii) *cameras* represented by $\tau \in \mathbb{R}^k$. Notations and setup are depicted in Figure 2.

We represent the geometry as the zero level set of a neural network (MLP) f,

$$\mathcal{S}_\theta = \left\{ \boldsymbol{x} \in \mathbb{R}^3 \mid f(\boldsymbol{x};\theta) = 0 \right\}, \tag{1}$$

with learnable parameters $\theta \in \mathbb{R}^m$. To avoid the everywhere 0 solution, f is usually regularized [37, 5]. We opt for f to model a signed distance function (SDF) to its zero level set $\mathcal{S}_\theta$ [42]. We enforce the SDF constraint using the implicit geometric regularization (IGR) [11], detailed later. SDF has two benefits in our context: First, it allows an efficient ray casting with the sphere tracing algorithm [12, 20]; and second, IGR enjoys implicit regularization favoring smooth and realistic surfaces.

Figure 2: Notations.

IDR forward model. Given a pixel, indexed by p, associated with some input image, let $R_p(\tau) = \{\boldsymbol{c}_p + t\boldsymbol{v}_p \mid t \geq 0\}$ denote the ray through pixel p, where $\boldsymbol{c}_p = \boldsymbol{c}_p(\tau)$ denotes the unknown center of the respective camera and $\boldsymbol{v}_p = \boldsymbol{v}_p(\tau)$ the direction of the ray (i.e., the vector pointing from $\boldsymbol{c}_p$ towards pixel p). Let $\hat{\boldsymbol{x}}_p = \hat{\boldsymbol{x}}_p(\theta, \tau)$ denote the first intersection of the ray R_p and the surface $\mathcal{S}_\theta$. The incoming radiance along R_p, which determines the rendered color of the pixel $L_p = L_p(\theta, \gamma, \tau)$, is a function of the surface properties at $\hat{\boldsymbol{x}}_p$, the incoming radiance at $\hat{\boldsymbol{x}}_p$, and the viewing direction $\boldsymbol{v}_p$. In turn, we make the assumptions that the surface property and incoming radiance are functions of the surface point $\hat{\boldsymbol{x}}_p$, and its corresponding surface normal $\hat{\boldsymbol{n}}_p = \hat{\boldsymbol{n}}_p(\theta)$, the viewing direction $\boldsymbol{v}_p$, and a global geometry feature vector $\hat{\boldsymbol{z}}_p = \hat{\boldsymbol{z}}_p(\hat{\boldsymbol{x}}_p; \theta)$. The IDR forward model is therefore:

$$L_p(\theta, \gamma, \tau) = M(\hat{\boldsymbol{x}}_p, \hat{\boldsymbol{n}}_p, \hat{\boldsymbol{z}}_p, \boldsymbol{v}_p; \gamma), \tag{2}$$

where M is a second neural network (MLP). We utilize L_p in a loss comparing L_p and the pixel input color I_p to simultaneously train the model's parameters θ, γ, τ. We next provide more details on the different components of the model in equation 2.

3.1 Differentiable intersection of viewing direction and geometry

Henceforth (up until section 3.4), we assume a fixed pixel p, and remove the subscript p notation to simplify notation. The first step is to represent the intersection point $\hat{\boldsymbol{x}}(\theta, \tau)$ as a neural network with parameters θ, τ. This can be done with a slight modification to the geometry network f.

Let $\hat{\boldsymbol{x}}(\theta, \tau) = \boldsymbol{c} + t(\theta, \boldsymbol{c}, \boldsymbol{v})\boldsymbol{v}$ denote the intersection point. As we are aiming to use $\hat{\boldsymbol{x}}$ in a gradient descent-like algorithm, all we need to make sure is that our derivations are correct in value and first derivatives at the current parameters, denoted by θ_0, τ_0; accordingly we denote $\boldsymbol{c}_0 = \boldsymbol{c}(\tau_0)$, $\boldsymbol{v}_0 = \boldsymbol{v}(\tau_0)$, $t_0 = t(\theta_0, \boldsymbol{c}_0, \boldsymbol{v}_0)$, and $\boldsymbol{x}_0 = \hat{\boldsymbol{x}}(\theta_0, \tau_0) = \boldsymbol{c}_0 + t_0\boldsymbol{v}_0$.

Lemma 1. *Let $\mathcal{S}_\theta$ be defined as in equation 1. The intersection of the ray $R(\tau)$ and the surface $\mathcal{S}_\theta$ can be represented by the formula*

$$\hat{\boldsymbol{x}}(\theta, \tau) = \boldsymbol{c} + t_0\boldsymbol{v} - \frac{\boldsymbol{v}}{\nabla_{\boldsymbol{x}} f(\boldsymbol{x}_0; \theta_0) \cdot \boldsymbol{v}_0} f(\boldsymbol{c} + t_0\boldsymbol{v}; \theta), \tag{3}$$

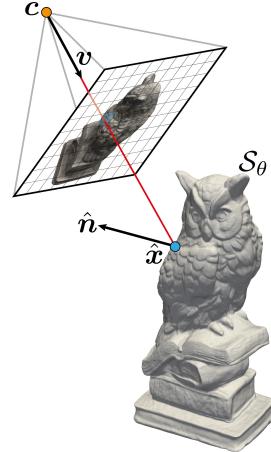*and is exact in value and first derivatives of θ and τ at $\theta = \theta_0$ and $\tau = \tau_0$.*

3

To prove this functional dependency of $\hat{\boldsymbol{x}}$ on its parameters, we use implicit differentiation [1, 40], that is, differentiate the equation $f(\hat{\boldsymbol{x}}; \theta) \equiv 0$ w.r.t. $\boldsymbol{v}, \boldsymbol{c}, \theta$ and solve for the derivatives of t. Then, it can be checked that the formula in equation 3 possess the correct derivatives. More details are in the supplementary. We implement equation 3 as a neural network, namely, we add two linear layers (with parameters $\boldsymbol{c}, \boldsymbol{v}$): one before and one after the MLP f. Equation 3 unifies the sample network formula in [1] and the differentiable depth in [40] and generalizes them to account for unknown cameras. The normal vector to $\mathcal{S}_\theta$ at $\hat{\boldsymbol{x}}$ can be computed by:

$$\hat{\boldsymbol{n}}(\theta, \tau) = \nabla_{\boldsymbol{x}} f(\hat{\boldsymbol{x}}(\theta, \tau), \theta) / \left\| \nabla_{\boldsymbol{x}} f(\hat{\boldsymbol{x}}(\theta, \tau), \theta) \right\|_2. \tag{4}$$

Note that for SDF the denominator is 1, so can be omitted.

3.2 Approximation of the surface light field

The surface light field radiance L is the amount of light reflected from $\mathcal{S}_\theta$ at $\hat{\boldsymbol{x}}$ in direction $-\boldsymbol{v}$ reaching $\boldsymbol{c}$. It is determined by two functions: The bidirectional reflectance distribution function (BRDF) describing the reflectance and color properties of the surface, and the light emitted in the scene (i.e., light sources).

The BRDF function $B(\boldsymbol{x}, \boldsymbol{n}, \boldsymbol{w}^o, \boldsymbol{w}^i)$ describes the proportion of reflected radiance (i.e., flux of light) at some wave-length (i.e., color) leaving the surface point $\boldsymbol{x}$ with normal $\boldsymbol{n}$ at direction $\boldsymbol{w}^o$ with respect to the incoming radiance from direction $\boldsymbol{w}^i$. We let the BRDF depend also on the normal $\boldsymbol{n}$ to the surface at a point. The light sources in the scene are described by a function $L^e(\boldsymbol{x}, \boldsymbol{w}^o)$ measuring the emitted radiance of light at some wave-length at point $\boldsymbol{x}$ in direction $\boldsymbol{w}^o$. The amount of light reaching $\boldsymbol{c}$ in direction $\boldsymbol{v}$ equals the amount of light reflected from $\hat{\boldsymbol{x}}$ in direction $\boldsymbol{w}^o = -\boldsymbol{v}$ and is described by the so-called rendering equation [21, 17]:

$$L(\hat{\boldsymbol{x}}, \boldsymbol{w}^o) = L^e(\hat{\boldsymbol{x}}, \boldsymbol{w}^o) + \int_\Omega B(\hat{\boldsymbol{x}}, \hat{\boldsymbol{n}}, \boldsymbol{w}^i, \boldsymbol{w}^o) L^i(\hat{\boldsymbol{x}}, \boldsymbol{w}^i)(\hat{\boldsymbol{n}} \cdot \boldsymbol{w}^i) \, d\boldsymbol{w}^i = M_0(\hat{\boldsymbol{x}}, \hat{\boldsymbol{n}}, \boldsymbol{v}), \tag{5}$$

where $L^i(\hat{\boldsymbol{x}}, \boldsymbol{w}^i)$ encodes the incoming radiance at $\hat{\boldsymbol{x}}$ in direction $\boldsymbol{w}^i$, and the term $\hat{\boldsymbol{n}} \cdot \boldsymbol{w}^i$ compensates for the fact that the light does not hit the surface orthogonally; Ω is the half sphere centered at $\hat{\boldsymbol{n}}$. The function M_0 represents the surface light field as a function of the local surface geometry $\hat{\boldsymbol{x}}, \hat{\boldsymbol{n}}$, and the viewing direction $\boldsymbol{v}$. This rendering equation holds for every light wave-length; as described later we will use it for the red, green and blue (RGB) wave-lengths.

We restrict our attention to light fields that can be represented by a continuous function M_0. We denote the collection of such continuous functions by $\mathcal{P} = \{M_0\}$ (see supplementary material for more discussion on $\mathcal{P}$). Replacing M_0 with a (sufficiently large) MLP approximation M (neural renderer) provides the light field approximation:

$$L(\theta, \gamma, \tau) = M(\hat{\boldsymbol{x}}, \hat{\boldsymbol{n}}, \boldsymbol{v}; \gamma). \tag{6}$$

Disentanglement of geometry and appearance requires the learnable M to approximate M_0 *for all* inputs $\boldsymbol{x}, \boldsymbol{n}, \boldsymbol{v}$ rather than memorizing the radiance values for a particular geometry. Given an arbitrary choice of light field function $M_o \in \mathcal{P}$ there exists a choice of weights $\gamma = \gamma_0$ so that M approximates M_0 for all $\boldsymbol{x}, \boldsymbol{n}, \boldsymbol{v}$ (in some bounded set). This can be proved using a standard universality theorem for MLPs (details in the supplementary). However, the fact that M *can* learn the correct light field function M_0 does not mean it is *guaranteed* to learn it during optimization. Nevertheless, being able to approximate M_0 for arbitrary $\boldsymbol{x}, \boldsymbol{n}, \boldsymbol{v}$ is a *necessary condition* for disentanglement of geometry (represented with f) and appearance (represented with M). We name this necessary condition $\mathcal{P}$-*universality*.

Necessity of viewing direction and normal. For M to be able to represent the correct light reflected from a surface point $\boldsymbol{x}$, i.e., be $\mathcal{P}$-universal, it has to receive as arguments also $\boldsymbol{v}, \boldsymbol{n}$. The viewing direction $\boldsymbol{v}$ is necessary even if we expect M to work for a fixed geometry; e.g., for modeling specularity. The normal $\boldsymbol{n}$, on the other hand, can be memorized by M as a function of $\boldsymbol{x}$. However, for disentanglement of geometry, i.e., allowing M to learn appearance independently from the geometry, incorporating the normal direction is also necessary. This can be seen in Figure 3: A renderer M without normal information will produce the same light estimation in cases (a)
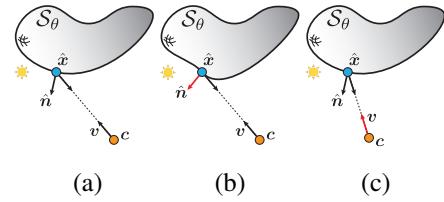

Figure 3: Neural renderers without $\boldsymbol{n}$ and/or $\boldsymbol{v}$ are not universal.

and (b), while a renderer M without viewing direction will produce the same light estimation in cases (a) and (c). In the supplementary we provide details on how these renderers fail to generate correct radiance under the Phong reflection model [8]. Previous works, e.g., [40], have considered rendering functions of implicit neural representations of the form $L(\theta, \gamma) = M(\hat{x}; \gamma)$. As indicated above, omitting n and/or v from M will result in a non-$\mathcal{P}$-universal renderer. In the experimental section we demonstrate that incorporating n in the renderer M indeed leads to a successful disentanglement of geometry and appearance, while omitting it impairs disentanglement.

Accounting for global light effects. $\mathcal{P}$-universality is a necessary conditions to learn a neural renderer M that can simulate appearance from the collection $\mathcal{P}$. However, $\mathcal{P}$ does not include global lighting effects such as secondary lighting and self-shadows. We further increase the expressive power of IDR by introducing a global feature vector $\hat{z}$. This feature vector allows the renderer to reason *globally* about the geometry $\mathcal{S}_\theta$. To produce the vector $\hat{z}$ we extend the network f as follows: $F(x; \theta) = [f(x; \theta), z(x; \theta)] \in \mathbb{R} \times \mathbb{R}^\ell$. In general, z can encode the geometry $\mathcal{S}_\theta$ relative to the surface sample x; z is fed into the renderer as $\hat{z}(\theta, \tau) = z(\hat{x}; \theta)$ to take into account the surface sample $\hat{x}$ relevant for the current pixel of interest p. We have now completed the description of the IDR model, given in equation 2.

3.3 Masked rendering

Another useful type of 2D supervision for reconstructing 3D geometry are masks; masks are binary images indicating, for each pixel p, if the object of interest occupies this pixel. Masks can be provided in the data (as we assume) or computed using, e.g., masking or segmentation algorithms. We would like to consider the following indicator function identifying whether a certain pixel is occupied by the rendered object (remember we assume some fixed pixel p):

$$S(\theta, \tau) = \begin{cases} 1 & R(\tau) \cap \mathcal{S}_\theta \neq \emptyset \\ 0 & \text{otherwise} \end{cases}$$

Since this function is not differentiable nor continuous in θ, τ we use an almost everywhere differentiable approximation:

$$S_\alpha(\theta, \tau) = \text{sigmoid}\left(-\alpha \min_{t \geq 0} f(c + tv; \theta)\right), \tag{7}$$

where $\alpha > 0$ is a parameter. Since, by convention, $f < 0$ inside our geometry and $f > 0$ outside, it can be verified that $S_\alpha(\theta, \tau) \xrightarrow{\alpha \to \infty} S(\theta, \tau)$. Note that differentiating equation 7 w.r.t. c, v can be done using the envelope theorem, namely $\partial_c \min_{t \geq 0} f(c + tv; \theta) = \partial_c f(c + t_* v; \theta)$, where t_* is an argument achieving the minimum, i.e., $f(c_0 + t_* v_0; \theta) = \min_{t \geq 0} f(c_0 + tv; \theta)$, and similarly for ∂_v. We therefore implement S_α as the neural network $\text{sigmoid}(-\alpha f(c + t_* v; \theta))$. Note that this neural network has exact value and first derivatives at $c = c_0$, and $v = v_0$.

3.4 Loss

Let $I_p \in [0,1]^3$, $O_p \in \{0,1\}$ be the RGB and mask values (resp.) corresponding to a pixel p in an image taken with camera $c_p(\tau)$ and direction $v_p(\tau)$ where $p \in P$ indexes all pixels in the input collection of images, and $\tau \in \mathbb{R}^k$ represents the parameters of all the cameras in scene. Our loss function has the form:

$$\text{loss}(\theta, \gamma, \tau) = \text{loss}_{\text{RGB}}(\theta, \gamma, \tau) + \rho\text{loss}_{\text{MASK}}(\theta, \tau) + \lambda\text{loss}_{\text{E}}(\theta) \tag{8}$$

We train this loss on mini-batches of pixels in P; for keeping notations simple we denote by P the current mini-batch. For each $p \in P$ we use the sphere-tracing algorithm [12, 20] to compute the first intersection point, $c_p + t_{p,0} v_p$, of the ray $R_p(\tau)$ and $\mathcal{S}_\theta$. Let $P^{\text{in}} \subset P$ be the subset of pixels p where intersection has been found and $O_p = 1$. Let $L_p(\theta, \gamma, \tau) = M(\hat{x}_p, \hat{n}_p, \hat{z}_p, v_p; \gamma)$, where $\hat{x}_p, \hat{n}_p$ is defined as in equations 3 and 4, and $\hat{z}_p = \hat{z}(\hat{x}_p; \theta)$ as in section 3.2 and equation 2. The RGB loss is

$$\text{loss}_{\text{RGB}}(\theta, \gamma, \tau) = \frac{1}{|P|} \sum_{p \in P^{\text{in}}} |I_p - L_p(\theta, \gamma, \tau)|, \tag{9}$$

where $|\cdot|$ represents the L_1 norm. Let $P^{\text{out}} = P \setminus P^{\text{in}}$ denote the indices in the mini-batch for which no ray-geometry intersection or $O_p = 0$. The mask loss is

$$\text{loss}_{\text{MASK}}(\theta, \tau) = \frac{1}{\alpha|P|} \sum_{p \in P^{\text{out}}} \text{CE}(O_p, S_{p,\alpha}(\theta, \tau)), \tag{10}$$
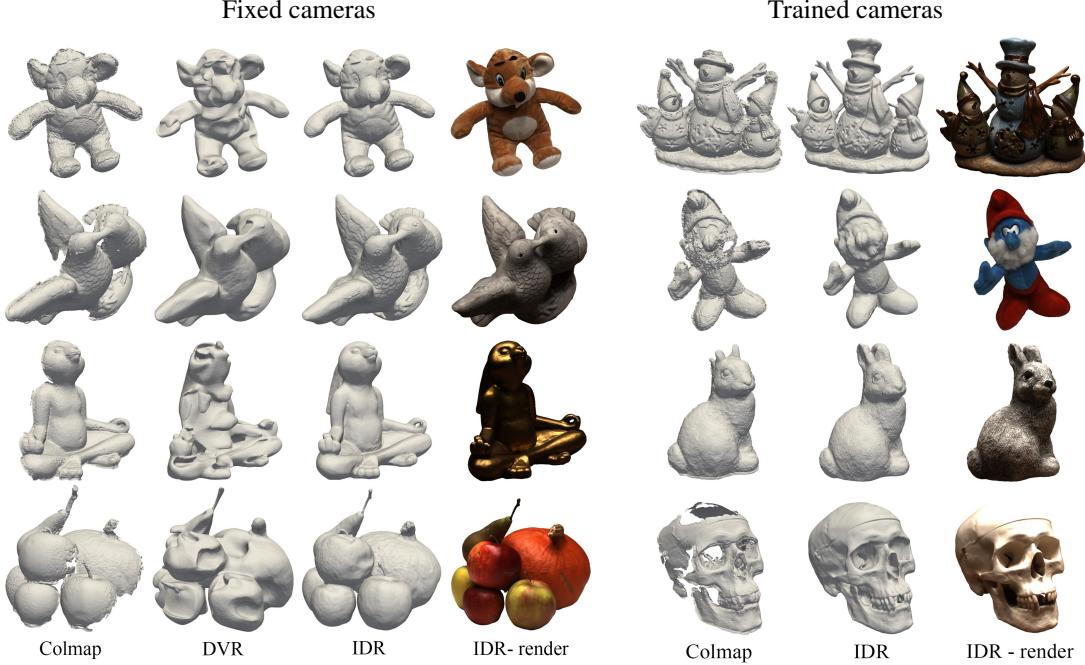
Figure 4: Qualitative results of multiview 3D surface reconstructions. Note the high fidelity of the IDR reconstructions and its realistic rendering.

where CE is the cross-entropy loss. Lastly, we enforce f to be approximately a signed distance function with Implicit Geometric Regularization (IGR) [11], i.e., incorporating the Eikonal regularization:

$$\text{loss}_{\text{E}}(\theta) = \mathbb{E}_{\boldsymbol{x}}\big(\|\nabla_{\boldsymbol{x}} f(\boldsymbol{x};\theta)\| - 1\big)^2 \tag{11}$$

where $\boldsymbol{x}$ is distributed uniformly in a bounding box of the scene.

Implementation details. The MLP $F(\boldsymbol{x};\theta) = (f(\boldsymbol{x};\theta), \boldsymbol{z}(\boldsymbol{x};\theta)) \in \mathbb{R} \times \mathbb{R}^{256}$ consists of 8 layers with hidden layers of width 512, and a single skip connection from the input to the middle layer as in [42]. We initialize the weights $\theta \in \mathbb{R}^m$ as in [2], so that $f(\boldsymbol{x}, \theta)$ produces an approximate SDF of a unit sphere. The renderer MLP, $M(\hat{\boldsymbol{x}}, \hat{\boldsymbol{n}}, \hat{\boldsymbol{z}}, \boldsymbol{v}; \gamma) \in \mathbb{R}^3$, consists of 4 layers, with hidden layers of width 512. We use the non-linear maps of [38] to improve the learning of high-frequencies, which are otherwise difficult to train for due to the inherent low frequency bias of neural networks [45]. Specifically, for a scalar $y \in \mathbb{R}$ we denote by $\boldsymbol{\delta}_k(y) \in \mathbb{R}^{2k}$ the vector of real and imaginary parts of $\exp(i 2^\omega \pi y)$ with $\omega \in [k]$, and for a vector $\boldsymbol{y}$ we denote by $\boldsymbol{\delta}_k(\boldsymbol{y})$ the concatenation of $\boldsymbol{\delta}_k(y_i)$ for all the entries of $\boldsymbol{y}$. We redefine F to obtain $\boldsymbol{\delta}_6(\boldsymbol{x})$ as input, i.e., $F(\boldsymbol{\delta}_6(\boldsymbol{x}); \theta)$, and likewise we redefine M to receive $\boldsymbol{\delta}_4(\boldsymbol{v})$, i.e., $M(\hat{\boldsymbol{x}}, \hat{\boldsymbol{n}}, \hat{\boldsymbol{z}}, \boldsymbol{\delta}_4(\boldsymbol{v}); \gamma)$. For the loss, equation 8, we set $\lambda = 0.1$ and $\rho = 100$. To approximate the indicator function with $S_\alpha(\theta, \tau)$, during training, we gradually increase α and by this constrain the shape boundaries in a coarse to fine manner: we start with $\alpha = 50$ and multiply it by a factor of 2 every 250 epochs (up to a total of 5 multiplications). The gradients in equations (11),(4) are implemented using using auto-differentiation. More details are in the supplementary.

4 Experiments

4.1 Multiview 3D reconstruction

We apply our multiview surface reconstruction model to real 2D images from the DTU MVS repository [18]. Our experiments were run on 15 challenging scans, each includes either 49 or 64 high resolution images of objects with a wide variety of materials and shapes. The dataset also contains ground truth 3D geometries and camera poses. We manually annotated binary masks for all 15 scans except for scans 65, 106 and 118 which are supplied by [40].

We used our method to generate 3D reconstructions in two different setups: (1) fixed ground truth cameras, and (2) trainable cameras with noisy initializations obtained with the linear method of [19]. In both cases we re-normalize the cameras so that their visual hulls are contained in the unit sphere.

	Trimmed Mesh				Watertight Mesh							
Scan	$\text{Colmap}_{trim=7}$		$\text{Furu}_{trim=7}$		$\text{Colmap}_{trim=0}$		$\text{Furu}_{trim=0}$		DVR [40]		IDR	
	Chamfer	PSNR	Chamfer	PSNR	Chamfer	PSNR	Chamfer	PSNR	Chamfer	PSNR	Chamfer	PSNR
24	**0.45**	**19.8**	0.51	19.2	**0.81**	20.28	0.85	20.35	4.10(4.24)	16.23(15.66)	1.63	**23.29**
37	**0.91**	**15.49**	1.03	14.91	2.05	15.5	**1.87**	14.86	4.54(4.33)	13.93(14.47)	1.87	**21.36**
40	**0.37**	**20.48**	0.44	19.18	0.73	20.71	0.96	20.46	4.24(3.27)	18.15(19.45)	0.63	**24.39**
55	**0.37**	20.18	0.4	**20.92**	1.22	20.76	1.10	21.36	2.61(0.88)	17.14(18.47)	0.48	**22.96**
63	**0.9**	**17.05**	1.28	15.41	1.79	20.57	2.08	16.75	4.34(3.42)	17.84(18.42)	1.04	**23.22**
65	**1.0**	**14.98**	1.22	13.09	1.58	14.54	2.06	13.53	2.81(1.04)	17.23(20.42)	0.79	**23.94**
69	**0.54**	18.56	0.72	**18.77**	1.02	21.89	1.11	**21.62**	2.53(1.37)	16.33(16.78)	0.77	20.34
83	**1.22**	**18.91**	1.61	16.58	3.05	**23.2**	2.97	20.06	2.93(2.51)	18.1(19.01)	1.33	21.87
97	1.08	12.18	1.37	**12.36**	1.4	18.48	1.63	18.32	3.03(2.42)	16.61(16.66)	1.16	22.95
105	**0.64**	**20.48**	0.83	19.68	2.05	21.3	1.88	20.21	3.24(2.42)	18.39(19.19)	0.76	22.71
106	**0.48**	15.76	0.70	**16.28**	1.0	22.33	1.39	22.64	2.51(1.18)	17.39(18.1)	0.67	22.81
110	**0.59**	**16.71**	0.87	16.53	1.32	18.25	1.45	17.88	4.80(4.32)	14.43(15.4)	0.9	21.26
114	**0.32**	**19.9**	0.42	19.69	0.49	20.28	0.69	20.09	3.09(1.04)	17.08(20.86)	0.42	**25.35**
118	**0.45**	23.21	0.59	**24.68**	0.78	25.39	1.10	26.02	1.63(0.91)	19.08(19.5)	0.51	23.54
122	**0.43**	24.48	0.53	**25.64**	1.17	25.29	1.16	25.95	1.58(0.84)	21.03(22.51)	0.53	**27.98**
Mean	**0.65**	**18.54**	0.84	18.19	1.36	20.58	1.49	20.01	3.20(2.28)	17.26(18.33)	0.9	**23.20**

Table 1: Multiview 3D reconstruction with *fixed* cameras, quantitative results for DTU dataset. For DVR we also present (in parentheses) the results with a partial set of images (with reduced reflectance) as suggested in [40].

Training each multi-view image collection proceeded iteratively. Each iteration we randomly sampled 2048 pixel from each image and derived their per-pixel information, including $(I_p, O_p, \boldsymbol{c}_p, \boldsymbol{v}_p), p \in P$. We then optimized the loss in equation 8 to find the geometry $\mathcal{S}_\theta$ and renderer network M. After training, we used the Marching Cubes algorithm [33] to retrieve the reconstructed surface from f.

Evaluation. We evaluated the quality of our 3D surface reconstructions using the formal surface evaluation script of the DTU dataset, which measures the standard Chamfer-L_1 distance between the ground truth and the reconstruction. We also report PSNR of train image reconstructions. We note that the ground truth geometry in the dataset has some noise, does not include watertight surfaces, and often suffers from notable missing parts, e.g., Figure 5 and Fig.7c of [40]. We compare to the following baselines: DVR [40] (for fixed cameras), Colmap [48] (for fixed and trained cameras) and Furu [9] (for fixed cameras). Similar to [40], for a fair comparison we cleaned the point clouds of Colmap and Furu using the input masks before running the Screened Poisson Surface Reconstruction (sPSR) [25] to get a watertight surface reconstruction. For completeness we also report their trimmed reconstructions obtained with the trim7 configuration of sPSR that contain large missing parts (see Fig. 5 middle) but performs well in terms of the Chamfer distance.

Quantitative results of the experiment with known fixed cameras are presented in Table 1, and qualitative results are in Figure 4 (left). Our model outperforms the baselines in the PSNR metric, and in the Chamfer metric, for watertight surface reconstructions. In Table 3 we compare the reconstructions obtained with unknown trained camera. Qualitative results for this setup are shown in Figure 4 (right). The relevant baseline here is the Colmap SFM [47]+MVS[48] pipeline.

GT   Colmap   IDR

Figure 5: Example of ground truth data (left).

In Figure 7 we further show the convergence of our cameras (rotation and translation errors sorted from small to large) from the initialization of [19] during training epochs along with Colmap's cameras. We note that our method simultaneously improves the cameras parameters while reconstructing accurate 3D surfaces, still outperforming the baselines for watertight reconstruction and PSNR in most cases; scan 97 is a failure case of our method. As can be seen in Figure 4, our 3D surface reconstruction are more complete with better signal to noise ratio than the baselines, while our renderings (right column in each part) are close to realistic.

Small number of cameras. We further tested our method on the Fountain-P11 image collections [52] provided with 11 high resolution images with associated GT camera parameters. In Table 2 we show a comparison to Colmap (trim7-sPSR) in a setup of unknown cameras (our method is roughly initialized with [19]). Note the considerable improvement in final camera accuracy over Colmap. Qualitative results are shown in Figure 6.
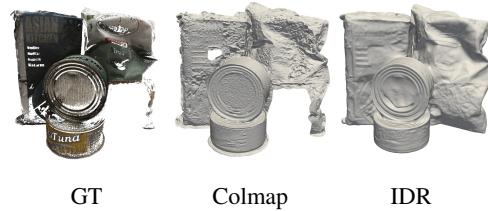
	R_{error}(deg)	t_{error}(mm)	PSNR
Colmap	0.03	2.86	21.99
IDR	**0.02**	**2.02**	**26.48**

Table 2: Fountain dataset: cameras accuracy and rendering quality.

Figure 6: Qualitative results for Fountain data set.

Scan	Trimmed Mesh		Watertight Mesh			
	$\text{Colmap}_{trim=7}$		$\text{Colmap}_{trim=0}$		IDR	
	Chamfer	PSNR	Chamfer	PSNR	Chamfer	PSNR
24	0.38	20.0	**0.73**	20.46	1.96	**23.16**
37	0.83	15.5	**1.96**	15.51	2.92	**20.39**
40	0.3	20.67	**0.67**	20.86	0.7	**24.45**
55	0.39	20.71	1.17	21.22	**0.4**	**23.57**
63	0.99	17.37	1.8	20.67	**1.19**	**24.97**
65	1.45	15.2	1.61	14.59	**0.77**	**22.6**
69	0.55	18.5	1.03	21.93	**0.75**	**22.91**
83	1.21	19.08	3.07	**23.43**	**1.42**	21.97
97	1.03	12.25	1.37	**18.67**	-	-
105	0.61	20.38	2.03	21.22	**0.96**	**22.98**
106	0.48	15.78	0.93	**22.23**	**0.65**	21.18
110	1.33	18.14	**1.53**	18.28	2.84	**18.65**
114	0.29	19.83	**0.46**	20.25	0.51	**25.19**
118	0.42	23.22	0.74	**25.42**	**0.50**	22.58
122	0.4	24.67	1.17	**25.44**	**0.62**	24.42
Mean	0.71	18.75	1.35	20.68	1.16	**22.79**

Table 3: Multiview 3D reconstruction with *trained* cameras, quantitative results for DTU dataset.
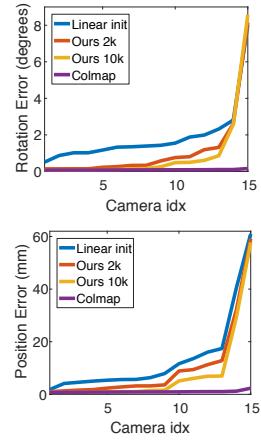

Figure 7: Cameras convergence for the DTU data set.

4.2 Disentangling geometry and appearance

To support the claim regarding the necessity of incorporating the surface normal, n, in the neural renderer, M, for disentangling geometry and appearance (see Section 3.2), we performed the following experiment: We trained two IDR models, each on a different DTU scene. Figure 8 (right) shows (from left to right): the reconstructed geometry; novel views produced with the trained renderer; and novel views produced after switching the renderers of the two IDR models. Figure 8 (left) shows the results of an identical experiment, however this time renderers are not provided with normal input, i.e., $M(\hat{x}, v, \hat{z}; \gamma)$. Note that using normals in the renderer provides a better geometry-appearance separation: an improved surface geometry approximation, as well as correct rendering of different geometries. Figure 9 depicts other combinations of appearance and geometry, where we render novel views of the geometry networks, f, using renderers, M, trained on different scenes.
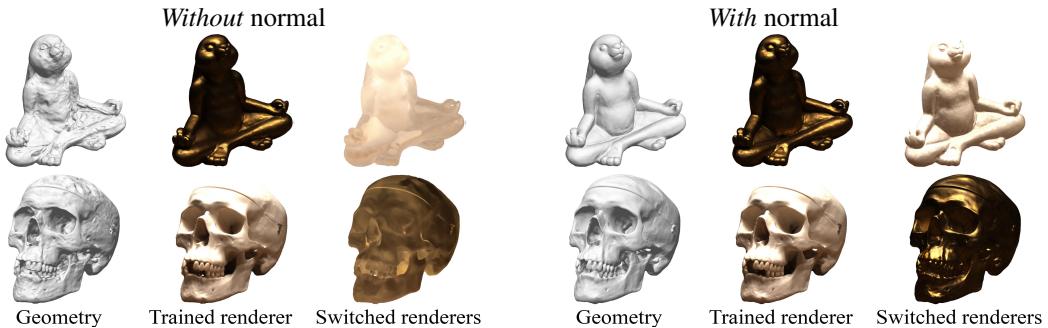

Figure 8: Incorporating normal in the renderer allows accurate geometry and appearance disentanglement: comparison of reconstructed geometry, novel view with trained renderer, and novel view with a different scene's renderer shown with and without normal incorporated in the renderer.
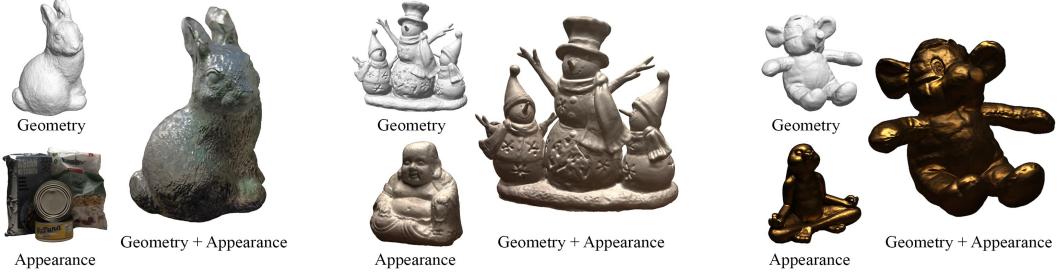
Figure 9: Transferring appearance to unseen geometry.

4.3 Ablation study

We used scan 114 of the DTU dataset to conduct an ablation study, where we removed various components of our renderer $M(\hat{\boldsymbol{x}}, \hat{\boldsymbol{n}}, \hat{\boldsymbol{z}}, \boldsymbol{v}; \gamma)$, including (see Figure 10): (a) the viewing direction $\boldsymbol{v}$; (b) the normal $\hat{\boldsymbol{n}}$; and (c) the feature vector, $\hat{\boldsymbol{z}}$. (d) shows the result with the full blown renderer M, achieving high detailed reconstruction of this marble stone figure (notice the cracks and fine details). In contrast, when the viewing direction, normal, or feature vector are removed the model tends to confuse lighting and geometry, which often leads to a deteriorated reconstruction quality.

In Figure 10 (e) we show the result of IDR training with fixed cameras set to the inaccurate camera initializations obtained with [19]; (f) shows IDR results when camera optimization is turned on. This indicates that the optimization of camera parameters together with the 3D geometry reconstruction is indeed significant.

| (a) | (b) | (c) | (d) | (e) | (f) |

Figure 10: Ablation study, see text for details.

5   Conclusions

We have introduced the Implicit Differentiable Renderer (IDR), an end-to-end neural system that can learn 3D geometry, appearance, and cameras from masked 2D images and noisy camera intializations. Considering only rough camera estimates allows for robust 3D reconstruction in realistic scenarios in which exact camera information is not available. One limitation of our method is that it requires a reasonable camera initialization and cannot work with, say random camera initialization. Interesting future work is to combine IDR with a neural network that predicts camera information directly from the images. Another interesting future work is to further factor the surface light field (M_0 in equation 5) into material (BRDF, B) and light in the scene (L^i). Lastly, we would like to incorporate IDR in other computer vision and learning applications such as 3D model generation, and learning 3D models from images in the wild.

Acknowledgments

Broader Impact

In our work we want to learn 3D geometry of the world from the abundant data of 2D images. In particular we allow high quality of 3D reconstruction of objects and scenes using only standard images. Applications of our algorithm could be anywhere 3D information is required, but only 2D images are available. This could be the case in: product design, entertainment, security, medical imaging, and more.

References

[1] Matan Atzmon, Niv Haim, Lior Yariv, Ofer Israelov, Haggai Maron, and Yaron Lipman. Controlling neural level sets. In *Advances in Neural Information Processing Systems*, pages 2032–2041, 2019.

[2] Matan Atzmon and Yaron Lipman. Sal: Sign agnostic learning of shapes from raw data. *arXiv preprint arXiv:1911.10414*, 2019.

[3] Neill DF Campbell, George Vogiatzis, Carlos Hernández, and Roberto Cipolla. Using multiple hypotheses to improve depth-maps for multi-view stereo. In *European Conference on Computer Vision*, pages 766–779. Springer, 2008.

[4] Wenzheng Chen, Huan Ling, Jun Gao, Edward Smith, Jaakko Lehtinen, Alec Jacobson, and Sanja Fidler. Learning to predict 3d objects with an interpolation-based differentiable renderer. In *Advances in Neural Information Processing Systems*, pages 9605–9616, 2019.

[5] Zhiqin Chen and Hao Zhang. Learning implicit fields for generative shape modeling. In *Proceedings of the IEEE Conference on Computer Vision and Pattern Recognition*, pages 5939–5948, 2019.

[6] Brian Curless and Marc Levoy. A volumetric method for building complex models from range images. In *Proceedings of the 23rd annual conference on Computer graphics and interactive techniques*, pages 303–312, 1996.

[7] Simon Donne and Andreas Geiger. Learning non-volumetric depth fusion using successive reprojections. In *Proceedings of the IEEE Conference on Computer Vision and Pattern Recognition*, pages 7634–7643, 2019.

[8] James D Foley, Foley Dan Van, Andries Van Dam, Steven K Feiner, John F Hughes, Edward Angel, and J Hughes. *Computer graphics: principles and practice*, volume 12110. Addison-Wesley Professional, 1996.

[9] Yasutaka Furukawa and Jean Ponce. Accurate, dense, and robust multiview stereopsis. *IEEE transactions on pattern analysis and machine intelligence*, 32(8):1362–1376, 2009.

[10] Kyle Genova, Forrester Cole, Aaron Maschinot, Aaron Sarna, Daniel Vlasic, and William T Freeman. Unsupervised training for 3d morphable model regression. In *Proceedings of the IEEE Conference on Computer Vision and Pattern Recognition*, pages 8377–8386, 2018.

[11] Amos Gropp, Lior Yariv, Niv Haim, Matan Atzmon, and Yaron Lipman. Implicit geometric regularization for learning shapes. *arXiv preprint arXiv:2002.10099*, 2020.

[12] John C Hart. Sphere tracing: A geometric method for the antialiased ray tracing of implicit surfaces. *The Visual Computer*, 12(10):527–545, 1996.

[13] Richard Hartley and Andrew Zisserman. *Multiple view geometry in computer vision*. Cambridge university press, 2003.

[14] Kurt Hornik, Maxwell Stinchcombe, and Halbert White. Universal approximation of an unknown mapping and its derivatives using multilayer feedforward networks. *Neural networks*, 3(5):551–560, 1990.

[15] Kurt Hornik, Maxwell Stinchcombe, Halbert White, et al. Multilayer feedforward networks are universal approximators. *Neural networks*, 2(5):359–366, 1989.

[16] Po-Han Huang, Kevin Matzen, Johannes Kopf, Narendra Ahuja, and Jia-Bin Huang. Deepmvs: Learning multi-view stereopsis. In *Proceedings of the IEEE Conference on Computer Vision and Pattern Recognition*, pages 2821–2830, 2018.

[17] David S Immel, Michael F Cohen, and Donald P Greenberg. A radiosity method for non-diffuse environments. *Acm Siggraph Computer Graphics*, 20(4):133–142, 1986.

[18] Rasmus Jensen, Anders Dahl, George Vogiatzis, Engil Tola, and Henrik Aanæs. Large scale multi-view stereopsis evaluation. In *2014 IEEE Conference on Computer Vision and Pattern Recognition*, pages 406–413. IEEE, 2014.

[19] Nianjuan Jiang, Zhaopeng Cui, and Ping Tan. A global linear method for camera pose registration. In *Proceedings of the IEEE International Conference on Computer Vision*, pages 481–488, 2013.

[20] Yue Jiang, Dantong Ji, Zhizhong Han, and Matthias Zwicker. Sdfdiff: Differentiable rendering of signed distance fields for 3d shape optimization. *arXiv preprint arXiv:1912.07109*, 2019.

[21] James T Kajiya. The rendering equation. In *Proceedings of the 13th annual conference on Computer graphics and interactive techniques*, pages 143–150, 1986.

[22] Yoni Kasten, Amnon Geifman, Meirav Galun, and Ronen Basri. Algebraic characterization of essential matrices and their averaging in multiview settings. In *Proceedings of the IEEE International Conference on Computer Vision*, pages 5895–5903, 2019.

[23] Hiroharu Kato, Yoshitaka Ushiku, and Tatsuya Harada. Neural 3d mesh renderer. In *Proceedings of the IEEE Conference on Computer Vision and Pattern Recognition*, pages 3907–3916, 2018.

[24] Michael Kazhdan, Matthew Bolitho, and Hugues Hoppe. Poisson surface reconstruction. In *Proceedings of the fourth Eurographics symposium on Geometry processing*, volume 7, 2006.

[25] Michael Kazhdan and Hugues Hoppe. Screened poisson surface reconstruction. *ACM Transactions on Graphics (ToG)*, 32(3):1–13, 2013.

[26] Diederik P Kingma and Jimmy Ba. Adam: A method for stochastic optimization. *arXiv preprint arXiv:1412.6980*, 2014.

[27] Vincent Leroy, Jean-Sébastien Franco, and Edmond Boyer. Shape reconstruction using volume sweeping and learned photoconsistency. In *Proceedings of the European Conference on Computer Vision (ECCV)*, pages 781–796, 2018.

[28] Tzu-Mao Li, Miika Aittala, Frédo Durand, and Jaakko Lehtinen. Differentiable monte carlo ray tracing through edge sampling. *ACM Transactions on Graphics (TOG)*, 37(6):1–11, 2018.

[29] Shichen Liu, Weikai Chen, Tianye Li, and Hao Li. Soft rasterizer: Differentiable rendering for unsupervised single-view mesh reconstruction. *arXiv preprint arXiv:1901.05567*, 2019.

[30] Shichen Liu, Shunsuke Saito, Weikai Chen, and Hao Li. Learning to infer implicit surfaces without 3d supervision. In *Advances in Neural Information Processing Systems*, pages 8293–8304, 2019.

[31] Shaohui Liu, Yinda Zhang, Songyou Peng, Boxin Shi, Marc Pollefeys, and Zhaopeng Cui. Dist: Rendering deep implicit signed distance function with differentiable sphere tracing. *arXiv preprint arXiv:1911.13225*, 2019.

[32] Matthew M Loper and Michael J Black. Opendr: An approximate differentiable renderer. In *European Conference on Computer Vision*, pages 154–169. Springer, 2014.

[33] William E Lorensen and Harvey E Cline. Marching cubes: A high resolution 3d surface construction algorithm. *ACM siggraph computer graphics*, 21(4):163–169, 1987.

[34] David G Lowe. Distinctive image features from scale-invariant keypoints. *International journal of computer vision*, 60(2):91–110, 2004.

[35] Matthew Matl. Pyrender code. `https://github.com/mmatl/pyrender`.

[36] Paul Merrell, Amir Akbarzadeh, Liang Wang, Philippos Mordohai, Jan-Michael Frahm, Ruigang Yang, David Nistér, and Marc Pollefeys. Real-time visibility-based fusion of depth maps. In *2007 IEEE 11th International Conference on Computer Vision*, pages 1–8. IEEE, 2007.

[37] Lars Mescheder, Michael Oechsle, Michael Niemeyer, Sebastian Nowozin, and Andreas Geiger. Occupancy networks: Learning 3d reconstruction in function space. In *Proceedings of the IEEE Conference on Computer Vision and Pattern Recognition*, pages 4460–4470, 2019.

[38] Ben Mildenhall, Pratul P Srinivasan, Matthew Tancik, Jonathan T Barron, Ravi Ramamoorthi, and Ren Ng. Nerf: Representing scenes as neural radiance fields for view synthesis. *arXiv preprint arXiv:2003.08934*, 2020.

[39] Michael Niemeyer. Dvr code. `https://github.com/autonomousvision/differentiable_volumetric_rendering`.

[40] Michael Niemeyer, Lars Mescheder, Michael Oechsle, and Andreas Geiger. Differentiable volumetric rendering: Learning implicit 3d representations without 3d supervision. *arXiv preprint arXiv:1912.07372*, 2019.

[41] Michael Oechsle, Michael Niemeyer, Lars Mescheder, Thilo Strauss, and Andreas Geiger. Learning implicit surface light fields. *arXiv preprint arXiv:2003.12406*, 2020.

[42] Jeong Joon Park, Peter Florence, Julian Straub, Richard Newcombe, and Steven Lovegrove. Deepsdf: Learning continuous signed distance functions for shape representation. In *Proceedings of the IEEE Conference on Computer Vision and Pattern Recognition*, pages 165–174, 2019.

[43] Adam Paszke, Sam Gross, Soumith Chintala, Gregory Chanan, Edward Yang, Zachary DeVito, Zeming Lin, Alban Desmaison, Luca Antiga, and Adam Lerer. Automatic differentiation in pytorch. 2017.

[44] Gernot Riegler, Ali Osman Ulusoy, Horst Bischof, and Andreas Geiger. Octnetfusion: Learning depth fusion from data. In *2017 International Conference on 3D Vision (3DV)*, pages 57–66. IEEE, 2017.

[45] Basri Ronen, David Jacobs, Yoni Kasten, and Shira Kritchman. The convergence rate of neural networks for learned functions of different frequencies. In *Advances in Neural Information Processing Systems*, pages 4763–4772, 2019.

[46] Shunsuke Saito, Zeng Huang, Ryota Natsume, Shigeo Morishima, Angjoo Kanazawa, and Hao Li. Pifu: Pixel-aligned implicit function for high-resolution clothed human digitization. In *Proceedings of the IEEE International Conference on Computer Vision*, pages 2304–2314, 2019.

[47] Johannes L. Schonberger and Jan-Michael Frahm. Structure-from-motion revisited. In *The IEEE Conference on Computer Vision and Pattern Recognition (CVPR)*, June 2016.

[48] Johannes L Schönberger, Enliang Zheng, Jan-Michael Frahm, and Marc Pollefeys. Pixelwise view selection for unstructured multi-view stereo. In *European Conference on Computer Vision*, pages 501–518. Springer, 2016.

[49] Johannes L. Schönberger. Colmap code. `https://colmap.github.io/`.

[50] Vincent Sitzmann, Michael Zollhöfer, and Gordon Wetzstein. Scene representation networks: Continuous 3d-structure-aware neural scene representations. In *Advances in Neural Information Processing Systems*, pages 1119–1130, 2019.

[51] Noah Snavely, Steven M Seitz, and Richard Szeliski. Photo tourism: exploring photo collections in 3d. In *ACM Siggraph 2006 Papers*, pages 835–846. 2006.

[52] Christoph Strecha, Wolfgang Von Hansen, Luc Van Gool, Pascal Fua, and Ulrich Thoennessen. On benchmarking camera calibration and multi-view stereo for high resolution imagery. In *2008 IEEE Conference on Computer Vision and Pattern Recognition*, pages 1–8. Ieee, 2008.

[53] Chengzhou Tang and Ping Liang Tan. Ba-net: Dense bundle adjustment networks. In *ICLR*, 2019.

[54] Engin Tola, Christoph Strecha, and Pascal Fua. Efficient large-scale multi-view stereo for ultra high-resolution image sets. *Machine Vision and Applications*, 23(5):903–920, 2012.

[55] Bill Triggs, Philip F McLauchlan, Richard I Hartley, and Andrew W Fitzgibbon. Bundle adjustment—a modern synthesis. In *International workshop on vision algorithms*, pages 298–372. Springer, 1999.

[56] Yao Yao, Zixin Luo, Shiwei Li, Tian Fang, and Long Quan. Mvsnet: Depth inference for unstructured multi-view stereo. In *Proceedings of the European Conference on Computer Vision (ECCV)*, pages 767–783, 2018.

[57] Yao Yao, Zixin Luo, Shiwei Li, Tianwei Shen, Tian Fang, and Long Quan. Recurrent mvsnet for high-resolution multi-view stereo depth inference. In *Proceedings of the IEEE Conference on Computer Vision and Pattern Recognition*, pages 5525–5534, 2019.

[58] Wang Yifan, Felice Serena, Shihao Wu, Cengiz Öztireli, and Olga Sorkine-Hornung. Differentiable surface splatting for point-based geometry processing. *ACM Transactions on Graphics (TOG)*, 38(6):1–14, 2019.

A Additional implementation details

A.1 Training details

We trained our networks using the ADAM optimizer [26] with a learning rate of $1e-4$ that we decrease by a factor of 2 at epochs 1000 and 1500. Each model was trained for $2K$ epochs. Training was done on a single Nvidia V-100 GPU, using PYTORCH deep learning framework [43]. Training time are 6.5 or 8 hours for 49 or 64 images, respectively. Rendering (inference) time: 30 seconds for 1200×1600 image with 100K pixel batches.

Images preprocessing. As in [50] we transform the RGB images such that each pixel is in the range $[-1, 1]^3$ by subtracting 0.5 and multiplying by 2.

A.2 Camera representation and initialization

We represent a camera by $\mathcal{C} = (\boldsymbol{q}, \boldsymbol{c}, \boldsymbol{K})$, where $\boldsymbol{q} \in \mathbb{R}^4$ is a quaternion vector representing the camera rotation, $\boldsymbol{c} \in \mathbb{R}^3$ represents the camera position, and $\boldsymbol{K} \in \mathbb{R}^{3 \times 3}$ is the camera's intrinsic parameters. Our cameras' parameters are $\tau = (\mathcal{C}_1, \dots, \mathcal{C}_N)$, where N is the numbers of cameras (also images) in the scene. Let $\boldsymbol{Q}(\boldsymbol{q}) \in \mathbb{R}^{3 \times 3}$ denote the rotation matrix corresponding to the quaternion $\boldsymbol{q}$. Then, for camera $\mathcal{C}_i$, $i \in [N]$, and a pixel p we have:

$$\boldsymbol{c}_p(\tau) = \boldsymbol{c}_i \tag{12}$$

$$\boldsymbol{v}_p(\tau) = \frac{1}{\left\| \boldsymbol{K}_i^{-1} \boldsymbol{p} \right\|_2} \boldsymbol{Q}(\boldsymbol{q}_i) \boldsymbol{K}_i^{-1} \boldsymbol{p}, \tag{13}$$

where $\boldsymbol{p} = (p_x, p_y, 1)^T$ is the pixel p in homogeneous coordinates.

In our experiments with unknown cameras, for each scene (corresponding to one 3D object) we generated relative motions between pairs of cameras using SIFT features matching [34] and robust essential matrix estimation (RANSAC), followed by a decomposition to relative rotation and relative translation [13]. We used these relative motions as inputs to the linear method of [19] to produce noisy cameras initialization for our method. We assume known intrinsics, as commonly assumed in calibrated SFM.

A.3 Architecture

Figure 11 visualize the IDR architecture. The gray blocks describe the input vectors, orange blocks for the output vectors, and each blue block describe a fully connected hidden layer with **softplus** activation ; a smooth approximation of **ReLU**: $x \mapsto \frac{1}{\beta} \ln(1 + e^{\beta x})$. We used $\beta = 100$. In the renderer network we used the **ReLU** activation between hidden layers and **tanh** for the output, to get valid color values. The grey block illustrate the use of equation 3.

As mentioned in the main paper, we initialize the weights of the implicit function $\theta \in \mathbb{R}^m$ as in [2], so that $f(\boldsymbol{x}, \theta)$ produces an approximate SDF of a unit sphere. To use the non-linear maps of [38], and still maintain the geometric initialization we implement the positional encoding embedding with the addition of concatenating identity embedding, that is: $\boldsymbol{\delta}'_k(\boldsymbol{y}) = [\boldsymbol{y}, \boldsymbol{\delta}_k(\boldsymbol{y})]$, where $\boldsymbol{\delta}_k(\boldsymbol{y})$ as defined in the section 3.4. Then, we zero out the weights coming out of everything except the linear basis function, to get the proper geometric initialization as in [2].
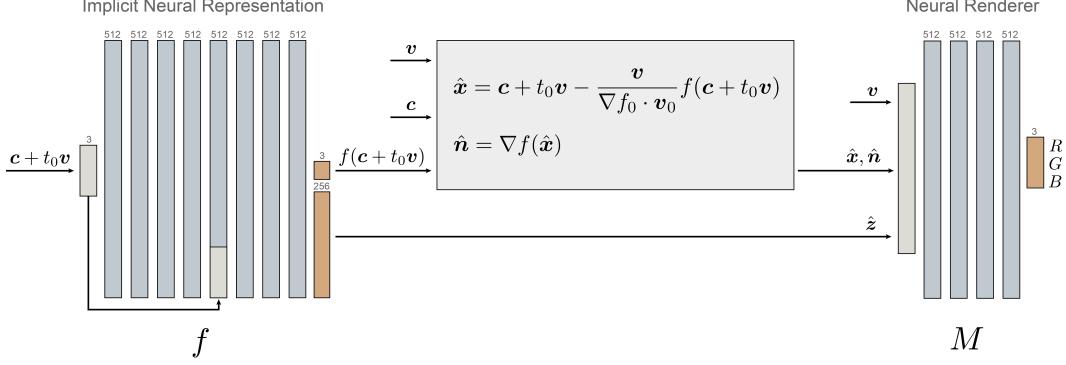
Figure 11: IDR architecture.

A.4 Ray marching algorithm

We denote by c the camera center and by $v \in \mathcal{S}$ the direction from c associated with a pixel on the image plane. During our training for each selected pixel, we perform ray tracing along the ray $\{c + tv \mid t \geq 0\}$ to find the corresponding first intersection point with $\mathcal{S}_\theta$ denoted by x_0. As $\mathcal{S}_\theta$ is defined by the zero level set of an approximated sign distance field f, we base our tracing method on the sphere tracing algorithm [12]: in each iteration, since the distance along the ray to x_0 is bounded by the current SDF value $f(c + tv)$, we march forward by enlarging the current t by $f(c + tv)$. We continue iterating until convergence, indicated by an SDF value below a threshold of 5e-5, or divergence, indicated by a step that reaches out of the unit sphere. As we assume the 3D object to be located inside the unit sphere, we start the sphere tracing algorithm at the first intersection point of the ray with the unit sphere as in [31].

We limit the number of sphere tracing steps to 10 in order to prevent long convergence cases e.g., when the ray passes very close to the surface without crossing it. Then, for non convergent rays, we run another 10 sphere tracing iterations starting from the second (i.e., farthest) intersection of the ray with the unit sphere and get $\bar{t}$. Similar to [40] we sample 100 equal sized steps between t to $\bar{t}$: $t < t_1 < \cdots < t_{100} < \bar{t}$ and find the first pair of consecutive steps t_i, t_{i+1} such that $\text{sign}(f(c + t_i v)) \neq \text{sign}(f(c + t_{i+1} v))$, i.e., a sign transition that describes the first ray crossing of the surface. Then, using t_i and t_j as initial values, we run 8 iterations of the secant algorithm to find an approximation for the intersection point x_0. The algorithm is performed in parallel on the GPU for multiple rays associated with multiple pixels.

For all pixels in P^{out} we select a point on the corresponding ray $c + t_* v$ for $\text{loss}_{\text{MASK}}$, where t_* is approximated by sampling uniformly 100 possible steps $\mathcal{T} = \{t_1, ..., t_{100}\}$ between the two intersection points of the ray with the unit sphere and taking $t_* = \arg\min_{t_i \in \mathcal{T}} f(c + t_i v)$.

All the 3D points resulted from the described process are used for equation 11 together with additionally 1024 points distributed uniformly in the bounding box of the scene.

A.5 Baselines methods running details

In our experiments we compared our method to Colmap [47],[48], DVR [40] and Furu [9]. We next describe implementation details for these baselines.

Colmap. We used the official Colmap implementation [49]. For unknown cameras, only the intrinsic camera parameters are given, and we used the "mapper" module to extract camera poses. For fixed known cameras the GT poses are given as inputs. For both setups we run their "feature_extractor", "exhaustive_matcher" , "point_triangulator", "patch_match_stereo" and "stereo_fusion" modules to generate point clouds. We also used their screened Poisson Surface Reconstruction (sPSR) for 3D mesh generation after cleaning the point clouds as described in Section 4.1. For rendering, we used their generated 3D meshes and cameras, and rendered images for each view using the "Pyrender" package [35].

DVR. We run DVR using the official Github code release [39]. In order to be compatible with this implementation, for each scene we used the cameras and the masks to normalize all the cameras such that the object is inside the unit cube. We applied DVR on all DTU scenes using the "ours_rgb" configuration. As mentioned in Table 1 (in the main paper), we reconstructed each model twice: with all the images in the dataset, and with all the images in the dataset that are not in the DVR "ignore list". We run their method for 5000 epochs and took the best model as they suggest. We further used their "generate" and "render" scripts for generating 3D meshes and rendering images respectively.

Furu. The point clouds generated by Furu are supplied by the DTU data set. We used Colmap's sPSR to generate meshes from the cleaned point clouds. As for Colmap we used "Pyrender" [35] to render their images.

A.6 Evaluation details

All the reported Chamfer distances are in millimeters and computed by averaging the accuracy and completeness measures, returned from DTU evaluation script, each represents one sided Chamfer-L_1 distance. The reported PSNR values (in dB) for each scan are averaged over the masked pixels of all the images. Camera accuracy represents the mean accuracy of camera positions (in mm) and camera rotations (in degrees) after L1 alignment with the GT.

B Additional results

B.1 Multiview 3D reconstruction

In Figure 12 we show a failure case (scan 37 from the DTU dataset). This case presents challenging thin metals parts which our method fails to fully reproduce especially with noisy cameras.

In Figure 14 we present qualitative results for 3D surface reconstruction with fixed GT cameras, whereas Figure 15 further presents qualitative results for the unknown cameras setup. An ablation study for training IDR with fixed noisy cameras compared to IDR's camera training mode initialized with the same noisy cameras is also presented in Figure 15. We refer the reader to a supplementary video named "IDR.mp4" that shows side by side our generated surfaces and rendered images from multiple views in the settings of unknown cameras.
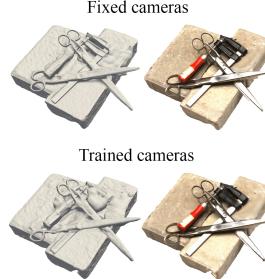

Fixed cameras

Trained cameras

Figure 12: Failure cases.

Unexpected lighting effects in the supplied video. In the original views (training images), the camera body occasionally occludes some light sources, casting temporary shadows on the object; see inset. Notice that in the video we move the camera (i.e., viewing direction) and not the object, therefore when the camera moves near such a view we see the projected shadow in the generated rendering.

B.2 Disentangling geometry and appearance

Figure 13 depicts other transformation of appearance to unseen geometry, where we render novel views of different trained geometries, using the renderer from the model trained on the golden bunny scene.

Figure 13: Transferring appearance from scan 110 (golden bunny) to unseen geometry.
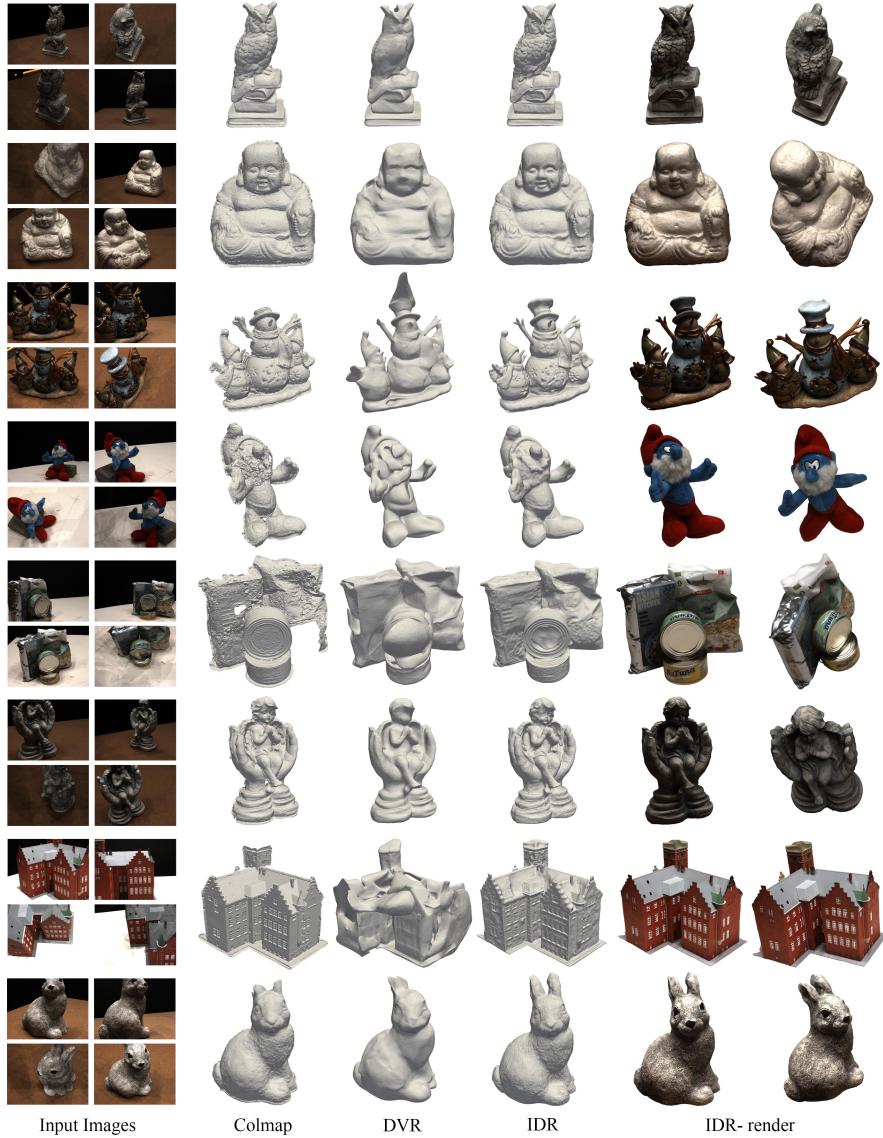
Figure 14: Qualitative results of multiview 3D surface reconstructions with fixed GT cameras for the DTU dataset. We present surface reconstructions generated by our method compared to the baseline methods. Our renderings from two novel views are presented as well.

B.3 PSNR on a held-out set of images

In our experiments the PSNR is computed over training images. We further performed an experiment where we held-out 10% of the images as test views, when using fixed GT cameras. Overall, we got 23.34 / 22.55 mean PSNR accuracy on the train / test images, respectively. Table 4 reports the per-scene accuracies.

Scan	24	37	40	55	63	65	69	83	97	105	106	110	114	118	122	Mean
PSNR(Test)	23.02	19.61	24.07	22.30	23.43	22.30	22.19	21.70	22.05	23.82	21.75	20.31	23.03	23.42	25.31	22.55
PSNR(Train)	24.13	21.02	24.65	23.51	24.81	23.33	22.74	21.80	23.29	24.36	22.04	20.32	23.89	23.72	26.45	23.34

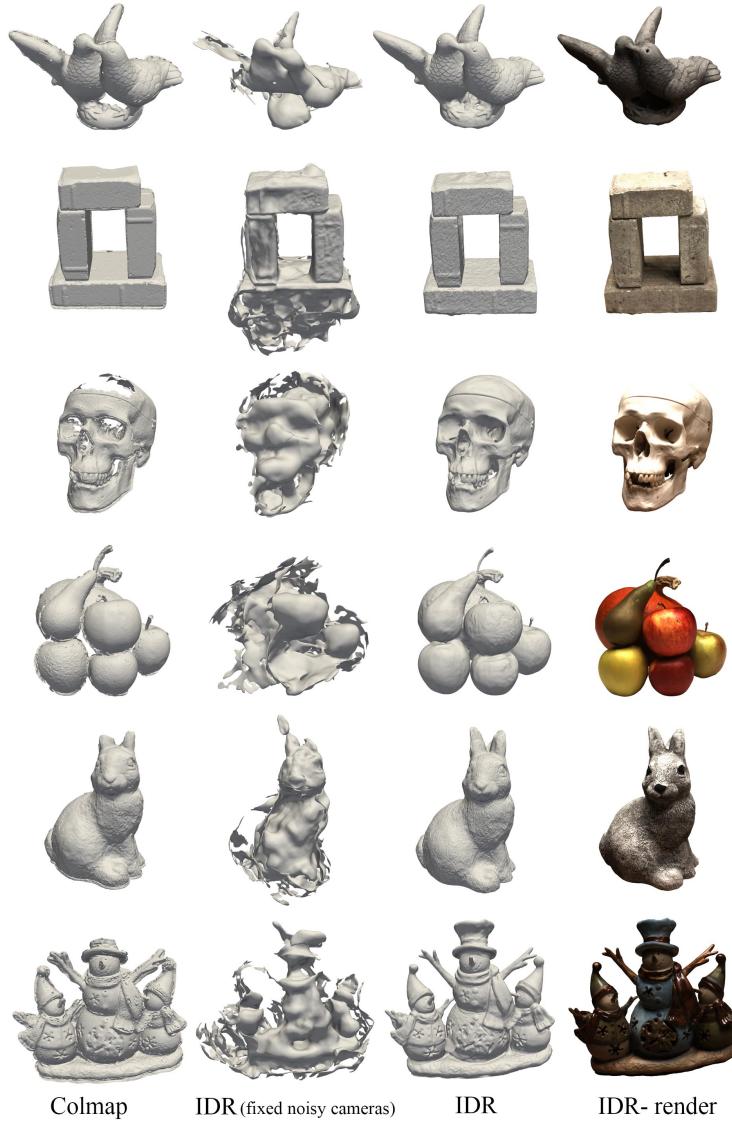Table 4: PSNR on a held-out set of images with fixed GT cameras.

15

Figure 15: Qualitative results for trained cameras setup. We also compare to IDR with fixed noisy cameras.

C Differentiable intersection of viewing direction and geometry (proof of Lemma 1)

We will use the notation of the main paper, repeated here for convenience: $\hat{\boldsymbol{x}}(\theta, \tau) = \boldsymbol{c}(\tau) + t(\theta, \boldsymbol{c}(\tau), \boldsymbol{v}(\tau))\boldsymbol{v}(\tau)$ denotes the first intersection point of the viewing ray $R_p(\tau)$ for some fixed pixel p and the geometry $\mathcal{S}_\theta$. We denote the current parameters by θ_0, τ_0; accordingly we denote $\boldsymbol{c}_0 = \boldsymbol{c}(\tau_0)$, $\boldsymbol{v}_0 = \boldsymbol{v}(\tau_0)$, and $t_0 = t(\theta_0, \boldsymbol{c}_0, \boldsymbol{v}_0)$. We also denote $\boldsymbol{x}_0 = \hat{\boldsymbol{x}}(\theta_0, \tau_0)$. Note that $\boldsymbol{x}_0 = \boldsymbol{c}_0 + t_0\boldsymbol{v}_0$ is the intersection point at the current parameters that is $R_p(\tau_0) \cap \mathcal{S}_{\theta_0}$.

To find the function dependence of $\hat{\boldsymbol{x}}$ on θ, τ we use implicit differentiation [1, 40]. That is we differentiate

$$f(\hat{\boldsymbol{x}}(\theta, \tau); \theta) \equiv 0 \tag{14}$$

w.r.t. its parameters. Since the functional dependence of $\boldsymbol{c}$ and $\boldsymbol{v}$ on τ is known (given in equations 12-13) it is sufficient to consider the derivatives of equation 14 w.r.t. $\theta, \boldsymbol{c}, \boldsymbol{v}$. Therefore we consider

$$f(\boldsymbol{c} + t(\theta, \boldsymbol{c}, \boldsymbol{v})\boldsymbol{v}; \theta) \equiv 0 \tag{15}$$

16

and differentiate w.r.t. θ, c, v. We differentiate w.r.t. c: (note that we use $\partial f / \partial x$ equivalently to $\nabla_x f$, which is used in the main paper)

$$\left(\frac{\partial f}{\partial \boldsymbol{x}}\right)^T \left(I + \boldsymbol{v}\left(\frac{\partial t}{\partial \boldsymbol{c}}\right)^T\right) = 0,$$

where $I \in \mathbb{R}^{3 \times 3}$ is the identity matrix, and $\boldsymbol{v}, \frac{\partial f}{\partial \boldsymbol{x}}, \frac{\partial t}{\partial \boldsymbol{c}} \in \mathbb{R}^3$ are column vectors. Rearranging and evaluating at $\theta_0, \boldsymbol{c}_0, \boldsymbol{v}_0$ we get

$$\frac{\partial t}{\partial \boldsymbol{c}}(\theta_0, \boldsymbol{c}_0, \boldsymbol{v}_0) = -\frac{1}{\left\langle \frac{\partial f}{\partial \boldsymbol{x}}(\boldsymbol{x}_0; \theta_0), \boldsymbol{v}_0 \right\rangle} \frac{\partial f}{\partial \boldsymbol{x}}(\boldsymbol{x}_0; \theta_0). \tag{16}$$

Differentiating w.r.t. $\boldsymbol{v}$:

$$\left(\frac{\partial f}{\partial \boldsymbol{x}}\right)^T \left(tI + \boldsymbol{v}\left(\frac{\partial t}{\partial \boldsymbol{v}}\right)^T\right) = 0,$$

Rearranging and evaluating at $\theta_0, \boldsymbol{c}_0, \boldsymbol{v}_0$ we get

$$\frac{\partial t}{\partial \boldsymbol{v}}(\theta_0, \boldsymbol{c}_0, \boldsymbol{v}_0) = -\frac{t_0}{\left\langle \frac{\partial f}{\partial \boldsymbol{x}}(\boldsymbol{x}_0; \theta_0), \boldsymbol{v}_0 \right\rangle} \frac{\partial f}{\partial \boldsymbol{x}}(\boldsymbol{x}_0; \theta_0). \tag{17}$$

Lastly, the derivatives w.r.t. θ are as in [40] and we give it here for completeness:

$$\left(\frac{\partial f}{\partial \boldsymbol{x}}\right)^T \boldsymbol{v} \frac{\partial t}{\partial \theta} + \frac{\partial f}{\partial \theta} = 0.$$

Reordering and evaluating at $\theta_0, \boldsymbol{v}_0, \boldsymbol{c}_0$ we get

$$\frac{\partial t}{\partial \theta}(\theta_0, \boldsymbol{c}_0, \boldsymbol{v}_0) = -\frac{1}{\left\langle \frac{\partial f}{\partial \boldsymbol{x}}(\boldsymbol{x}_0; \theta_0), \boldsymbol{v}_0 \right\rangle} \frac{\partial f}{\partial \theta}(\boldsymbol{x}_0; \theta_0) \tag{18}$$

Now consider the formula

$$t(\theta, \boldsymbol{c}, \boldsymbol{v}) = t_0 - \frac{1}{\left\langle \frac{\partial f}{\partial \boldsymbol{x}}(\boldsymbol{x}_0; \theta_0), \boldsymbol{v}_0 \right\rangle} f(\boldsymbol{c} + t_0\boldsymbol{v}; \theta). \tag{19}$$

Evaluating at $\theta_0, \boldsymbol{c}_0, \boldsymbol{v}_0$ we get $t(\theta_0, \boldsymbol{c}_0, \boldsymbol{v}_0) = t_0$ since $f(\boldsymbol{x}_0; \theta_0) = 0$. Furthermore, differentiating t w.r.t. $\boldsymbol{c}, \boldsymbol{v}, \theta$ and evaluating at $\boldsymbol{c}_0, \boldsymbol{v}_0, \theta_0$ we get the same derivatives as in equations 16, 17, and 18. Plugging equation 19 into $\hat{\boldsymbol{x}}(\theta, \boldsymbol{c}, \boldsymbol{v}) = \boldsymbol{c} + t(\theta, \boldsymbol{c}, \boldsymbol{v})\boldsymbol{v}$ we get the formula,

$$\hat{\boldsymbol{x}}(\theta, \tau) = \boldsymbol{c} + t_0\boldsymbol{v} - \frac{\boldsymbol{v}}{\left\langle \frac{\partial f}{\partial \boldsymbol{x}}(\boldsymbol{x}_0; \theta_0), \boldsymbol{v}_0 \right\rangle} f(\boldsymbol{c} + t_0\boldsymbol{v}; \theta), \tag{20}$$

that coincide in value and first derivatives with the first intersection points at the current parameters $\theta_0, \boldsymbol{c}_0, \boldsymbol{v}_0$; equation 20 can be implemented directly by adding a linear layer in the entrance to the network f and a linear layer at its output.

D Restricted surface light field model $\mathcal{P}$

We restrict our attention to light fields that can be represented by a *continuous* function M_0. We denote the collection of such continuous functions by $\mathcal{P} = \{M_0\}$.

This model includes many common materials and lighting conditions such as the popular Phong model [8]:

$$L(\hat{\boldsymbol{x}}, \boldsymbol{w}^o) = k_d O_d I_a + k_d O_d I_d \left(\hat{\boldsymbol{n}} \cdot \frac{\boldsymbol{\ell} - \hat{\boldsymbol{x}}}{\|\boldsymbol{\ell} - \hat{\boldsymbol{x}}\|}\right)_+ + k_s O_s I_d \left(\hat{\boldsymbol{r}} \cdot \frac{\boldsymbol{\ell} - \hat{\boldsymbol{x}}}{\|\boldsymbol{\ell} - \hat{\boldsymbol{x}}\|}\right)_+^{n_s}, \tag{21}$$

where $(a)_+ = \max\{a, 0\}$; k_d, k_s are the diffuse and specular coefficients, I_a, I_d are the ambient and point light source colors, O_d, O_s are the diffuse and specular colors of the surface, $\boldsymbol{\ell} \in \mathbb{R}^3$ is the location of a point light source, $\hat{\boldsymbol{r}} = -(\boldsymbol{I} - 2\hat{\boldsymbol{n}}\hat{\boldsymbol{n}}^T)\boldsymbol{w}^o$ the reflection of the viewing direction $\boldsymbol{w}^o = -\boldsymbol{v}$ with respect to the normal $\hat{\boldsymbol{n}}$, and n_s is the specular exponent.

Note, that the family $\mathcal{P}$, however, does not include all possible lighting conditions. It excludes, for example, self-shadows and second order (or higher) light reflections as L^i is independent of the geometry $\mathcal{S}_\theta$.

D.1 $\mathcal{P}$-Universality of renderer

We consider renderer of the form $M(\boldsymbol{x}, \boldsymbol{n}, \boldsymbol{v}; \gamma)$, where M is an MLP, and show it can approximate the correct light field function $M_0(\boldsymbol{x}, \boldsymbol{n}, \boldsymbol{v})$ for all $(\boldsymbol{x}, \boldsymbol{n}, \boldsymbol{v})$ contained in some compact set $\mathcal{K} \subset \mathbb{R}^9$. Indeed, for some arbitrary and fixed $\epsilon > 0$ the universal approximation theorem for MLPs (see [15] and [14] for approximation including derivatives) guarantees the existence of parameters $\gamma \in \mathbb{R}^n$ so that $\max_{(\boldsymbol{x}, \boldsymbol{n}, \boldsymbol{v}) \in \mathcal{K}} |M(\boldsymbol{x}, \boldsymbol{n}, \boldsymbol{v}; \gamma) - M_0(\boldsymbol{x}, \boldsymbol{n}, \boldsymbol{v})| < \epsilon$.

D.2 View direction and normal are necessary for $\mathcal{P}$-universality.

We will next prove that taking out $\boldsymbol{v}$ or $\boldsymbol{n}$ from the renderer M will make this model not $\mathcal{P}$-universal. Assume $\mathcal{S}_\theta$ is expressive enough to change the normal direction $\hat{\boldsymbol{n}}$ arbitrarily at a point $\hat{\boldsymbol{x}}$; for example, even a linear classifier $f(\boldsymbol{x}; \boldsymbol{a}, b) = \boldsymbol{a}^T \boldsymbol{x} + b$ would do. We will use the Phong model (equation 21) to prove the claims; the Phong model is in $\mathcal{P}$ as discussed above. We first consider the removal of the normal component $\hat{\boldsymbol{n}}$ from the renderer, i.e., $M(\hat{\boldsymbol{x}}, \boldsymbol{v}; \gamma)$ is the approximated light field radiance arriving at $\boldsymbol{c}$ in direction $\boldsymbol{v}$ as predicted by the renderer. Consider the setting shown in Figure 3 (a) and (b) (in the main paper): In both cases $M(\hat{\boldsymbol{x}}, \boldsymbol{v}; \gamma)$ yields the same value although changing the normal direction at $\hat{\boldsymbol{x}}$ will produce, under the Phong model, a different light amount at $\boldsymbol{c}$.

Similarly, consider a renderer with the viewing direction, $\boldsymbol{v}$, removed, i.e., $M(\hat{\boldsymbol{x}}, \hat{\boldsymbol{n}}; \gamma)$, and Figure 3 (a) and (c): In both cases $M(\hat{\boldsymbol{x}}, \hat{\boldsymbol{n}}; \gamma)$ produces the same value although, under the Phong model, the reflected light can change when the point of view changes. That is, we can choose light position $\boldsymbol{\ell}$ in equation 21 so that different amount of light reaches $\boldsymbol{c}$ at direction $\boldsymbol{v}$.

We have shown that renderers with no access to $\hat{\boldsymbol{n}}$ and/or $\boldsymbol{v}$ would necessarily fail (at-least in some cases) predicting the correct light amount reaching $\boldsymbol{c}$ in direction $\boldsymbol{v}$ when these and the geometry is able to change, hence are not universal.